Electronic supplementary information (ESI)

Mechanically robust ultrathin nanofibrous films by using microfluidic-based continuous printing

*Xiao Chen,†abc Jiaqing Su,†b Sha Cheng,b Cheng Huang,b Chunxia Zhao,ab Chao Teng*d and Pengchao Zhang*abc*

a. Hubei Longzhong Laboratory, Wuhan University of Technology Xiangyang Demonstration Zone, Xiangyang 441000, China

b. Key Laboratory of Advanced Technology for Materials Synthesis and Processing, School of Materials Science and Engineering, Wuhan University of Technology, Wuhan 430070, China

c. Sanya Science and Education Innovation Park, Wuhan University of Technology, Sanya 572024, China

d. College of Materials Science and Engineering, Qingdao University of Science and Technology, Qingdao 266042, China

† These authors contribute equally to the work.

Experimental section:

The atomic force microscopy (AFM) was performed on a FastScan Scanning Probe Microscopy (Bruker) with ScanAsyst in air mode at room temperature with scan areas of 1×1 μm^2, and 20×20 μm^2. The nanoindentation was carried on Hysitron TI 980 (Bruker) with a depth of 300 nm for the indentation.

The Raman analysis was performed by using labRAM Odyssey (Horiba) with a 532 nm source and a scan range from 50 to 4000 cm^{-1}. The X-ray diffraction (XRD) analysis was carried on Rigaku Minifiex 600/600-C with a Cu Ka radiation source, which the scanning range was 5°–90°, the scanning rate was 5°/min.

The small angle X-ray scattering was performed on Xeuss 3.0 SAXS/WAXS with model Eiger2R 1M, which used a Cu source with an 8.05 keV X-ray, the wavelength is 1.54189 Å. The measurement vacuum pressure was < 1 mbar, while the distance between detector and sample was 1200 mm.

The ANF films were fabricated by adjusting the proton concentration in the coagulation bath, which various pH were chosen as 6, 2, and 1 corresponding to the deionized water, 5 wt% acetic acid, and 10 wt% acetic acid solutions, respectively.

For heat treatment, both microfluidic and casted ANF films were placed in the oven for 200 ℃ with 2 hours. For high humidity condition, both microfluidic and casted ANF films were placed near the water bath under a sealed environment, which the water bath has heated to 40 ℃ for 2 hours. All samples were tested by tensile testing after the treatments.

Electrochemical testing: The prepared microfluidic ANF membranes were placed between electrochemical system. A pair of Ag/AgCl electrodes were used for detecting the current responses the microfluidic ANF membranes. The testing area of microfluidic ANF membranes was about 0.03 mm^2. Using three NaCl concentration gradients to explore the salinity gradient conversion ability of ANF microfluidic membranes. The low-concentration side was fixed at 0.01 M, and the high concentration side is fixed at was varied between 0.05 - 5 M. The output power density of the membrane can be calculated from the current displayed on the Keithley 2450 source meter.
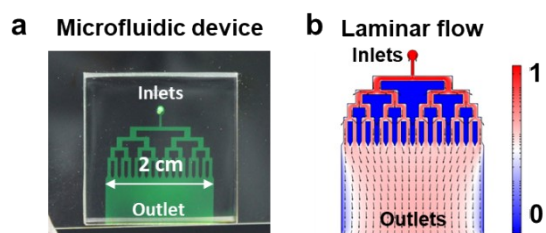
Supporting results:

Fig. S1. Images of (a) microfluidic devices and (b) the modelling of laminar flow.
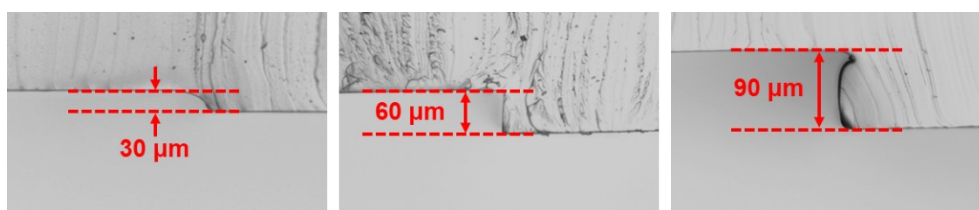

Fig. S2. Optical images of microfluidic devices with different microchannel heights.
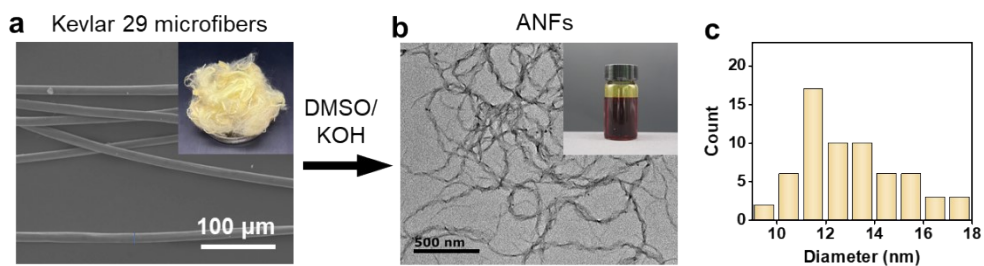

Fig. S3. The fabricated ANF solution. (a) Optical and SEM images of Kevlar 29 microfibers.

(b) Optical image of the ANF solution and TEM image of the aramid nanofibers. (c)
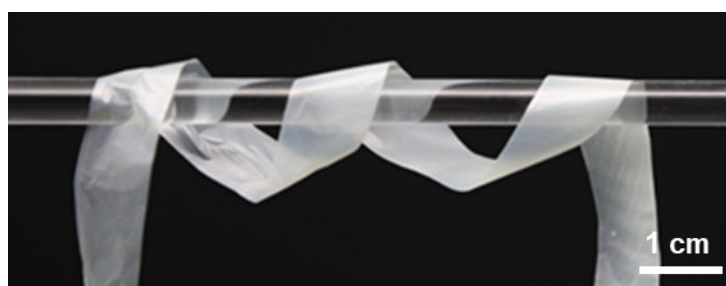
Statistical data showing the diameter of ANF.

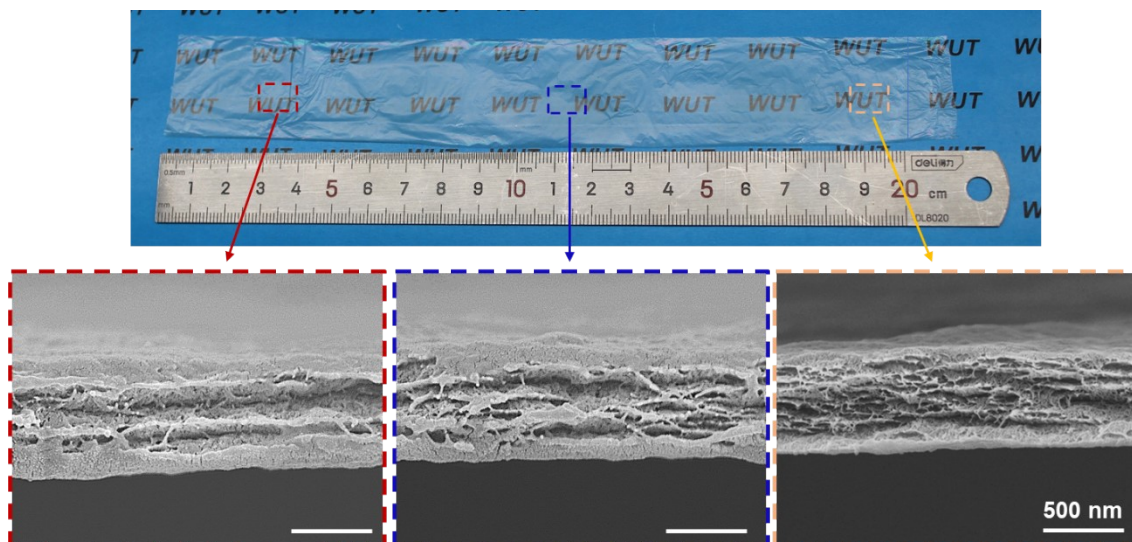**Fig. S4.** Flexibility of the prepared ANF films.

Fig. S5. The uniformity of the prepared ultrathin ANF films.
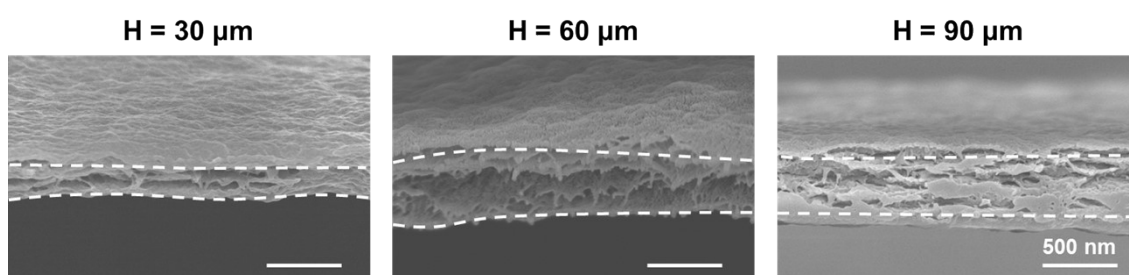

Fig. S6. SEM images of the ultrathin ANF films prepared at different microchannel heights.
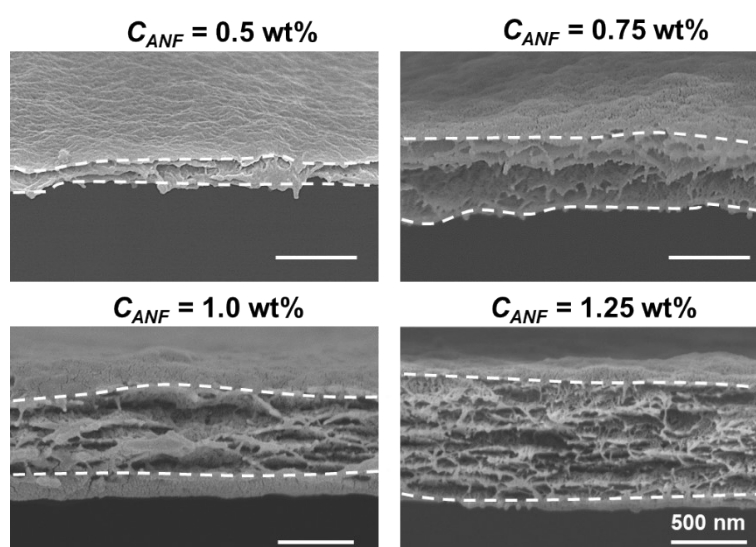

Fig. S7. SEM images of the ultrathin ANF films prepared using solutions with different
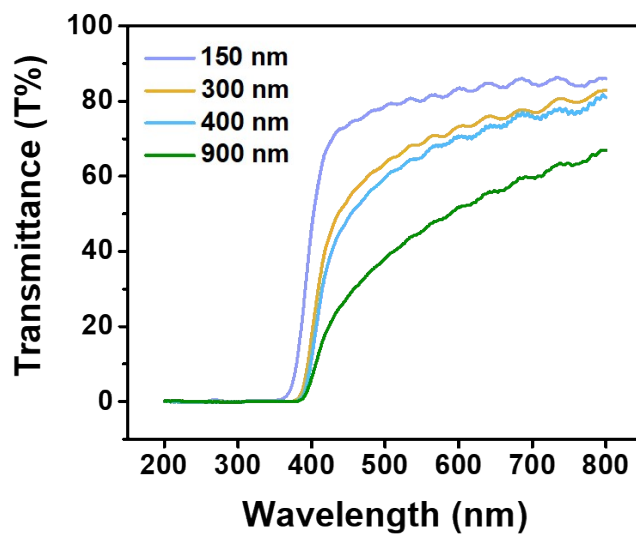
concentrations of ANF (C_{ANF}).

4

Fig. S8. Ultraviolet-visible spectra of the ultrathin ANF films with different thickness.
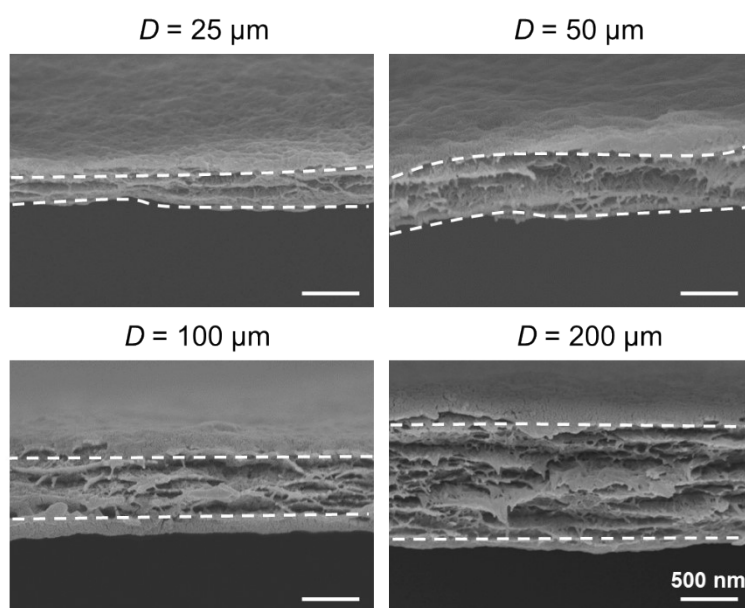

Fig. S9. SEM images of the ultrathin ANF films prepared by the doctor blade casting method with different distance (*D*) between the blade and substrate. The concentration of ANF was 1.0 wt%.
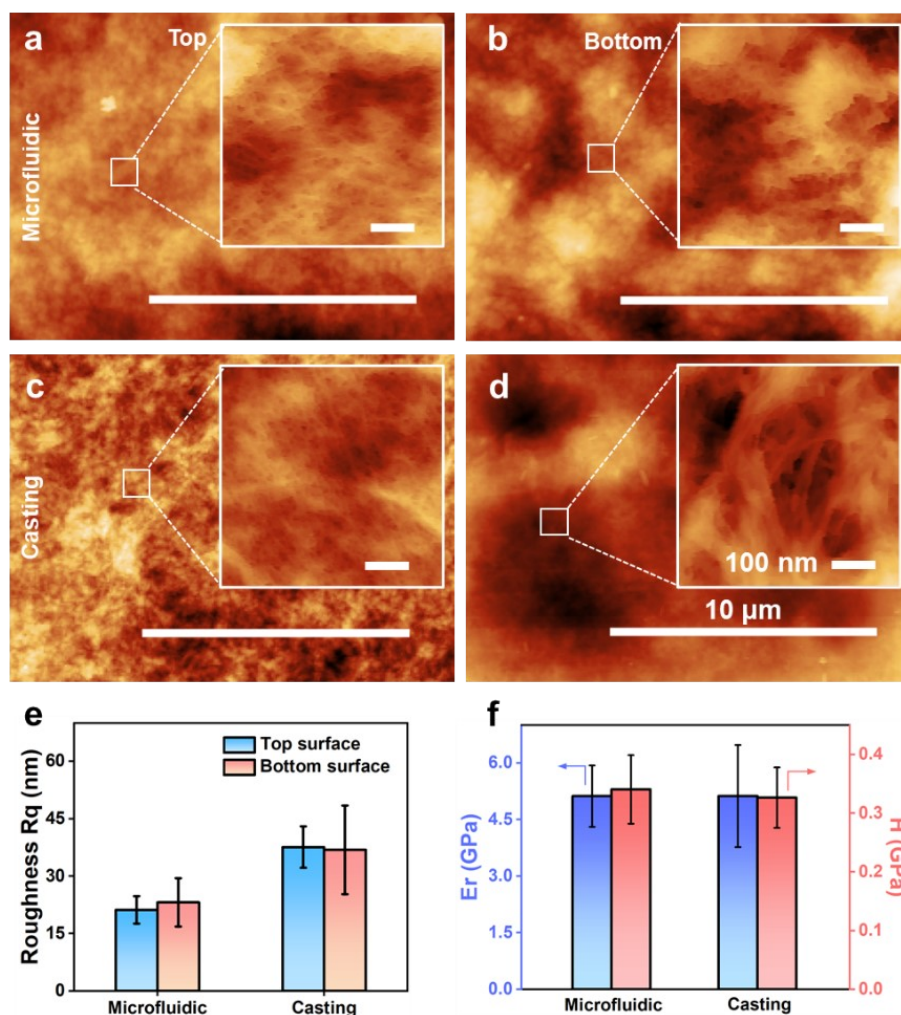
Fig. S10. (a-d) AFM images for microfluidic and casted ANF films for both top and bottom sides. (e) The roughness Rq values which are calculated from AFM images. (f) The nanoindentation results for modulus (Er) and hardness (H) from microfluidic and casted ANF films.
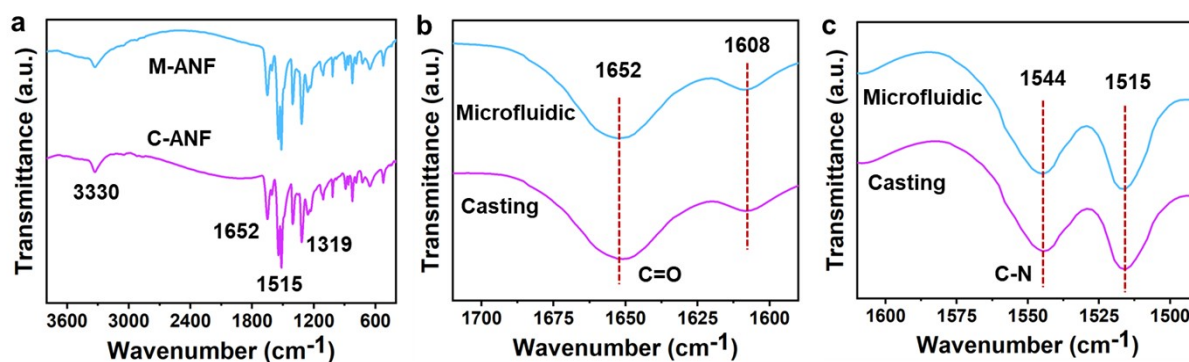

Fig. S11. FTIR spectra of the ultrathin ANF films from microfluidic-based printing and casting methods. (a) Whole spectra. (b) Spectra range from 1600 to 1700 cm^{-1}. (c) Spectra range from 1500 to 1600 cm^{-1}. Both methods indicate similar N-H/O-H stretching (3330 cm^{-1}), C=O stretching (1652 cm^{-1}), and C-N stretching vibrations (1544 cm^{-1}).
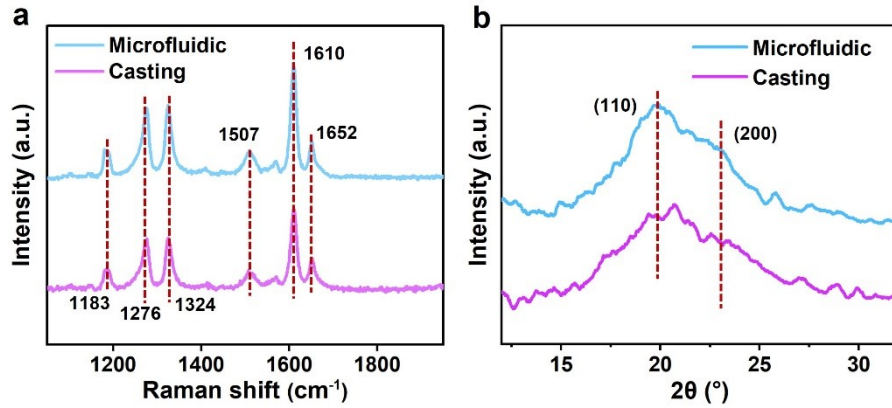
Fig. S12. (a) The Raman spectra for ANF films from microfluidic-based printing and casting methods, peaks located at 1183, 1276, 1507, and 1610 cm^{-1} contributed to the C-C ring stretching vibration, while 1324 cm^{-1} was based on C-H in-plane bending vibration, and 1570 and 1652 cm^{-1} were related to N-H bending and C-N stretching (C=O stretching vibration). (b) The XRD spectra for ANF films from the both methods, (110) is located at 19.9° and a shoulder as (200) is located at 23.1°. The weak (200) peak was resulted from the dissociation of hydrogen bonding between fiber molecular chains, the remained (100) represented as the benzene ring in the molecular chain.[1] ANF films from both methods suggest same spectra for Raman and XRD, indicating the high stability of molecular and crystalline structures of nanofibers are not affected by fabrication methods.
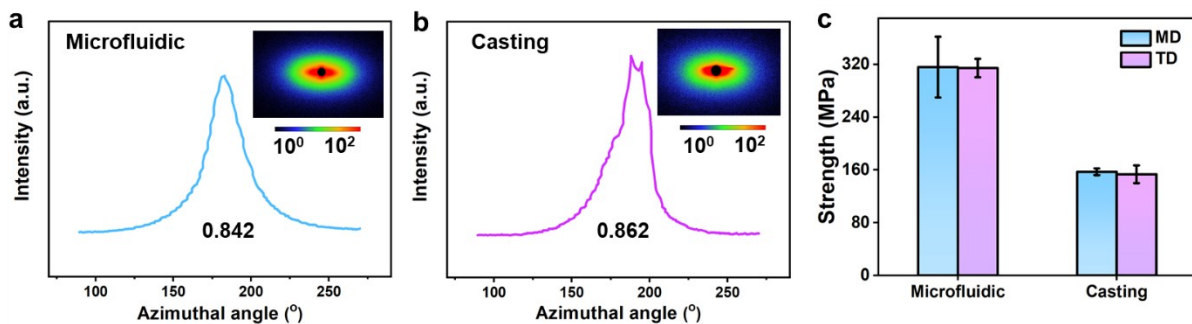

Fig. S13. (a-b) The small angle X-ray scattering results for ANF films from microfluidic-based printing and casting methods. (c) The MD and TD tensile strengths for ANF films from microfluidic-based printing and casting methods, showing same strength in both directions which indicates the random alignment for nanofibers from the surface side of the films.
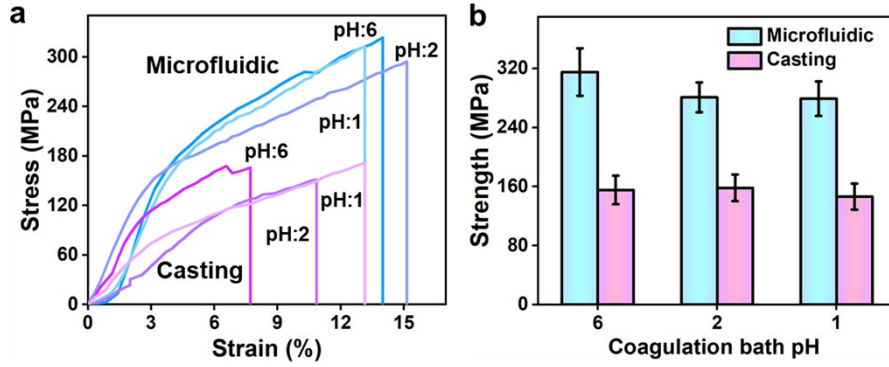
Fig. S14. (a) The stress-strain curves for ANF films under various pH of the coagulation bath. (b) The strength for ANF films from microfluidic-based printing and casting methods. The pKa for the ANF in the DMSO/KOH solution is around 19 – 29, which can result deprotonation to obtain the nanofibers.[2] The coagulation baths from water and acetic acid solutions provide pKa around 14 and less than 10, respectively. Hence, the coagulation bath can provide protons for driving the protonation of ANFs. When the pKa of coagulation bath above the pKa of the nanofibers as the pH increased to 10, the protonation will be slow down as discussed elsewhere.[3] Moreover, the resulted tensile strength and Young's modulus were dropped due to the loose structure from the slow protonation. Therefore, the protonation is a key factor for film formation, which assisted with microfluidic printing to fabricate the dense and strong thin films.
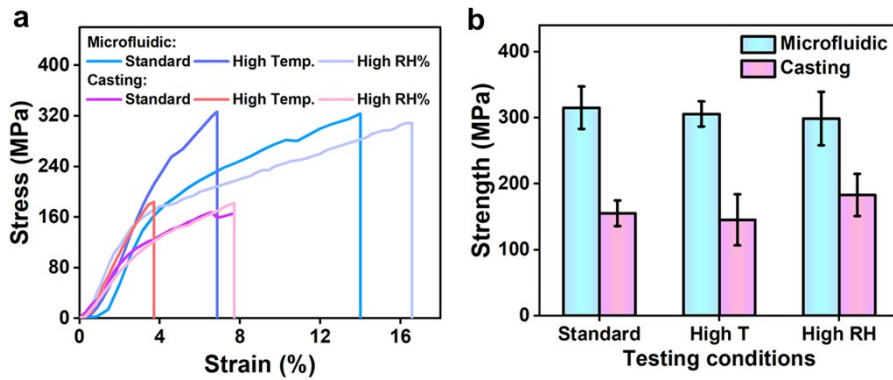

Fig. S15. (a) The stress and strain curves for ANF films from microfluidic-based printing and casting methods under standard testing condition, 200℃ treatments for 2 h, around 90% RH for 2 h, (b) the strength for aforementioned conditions for ANF films from microfluidic-based printing and casting methods.
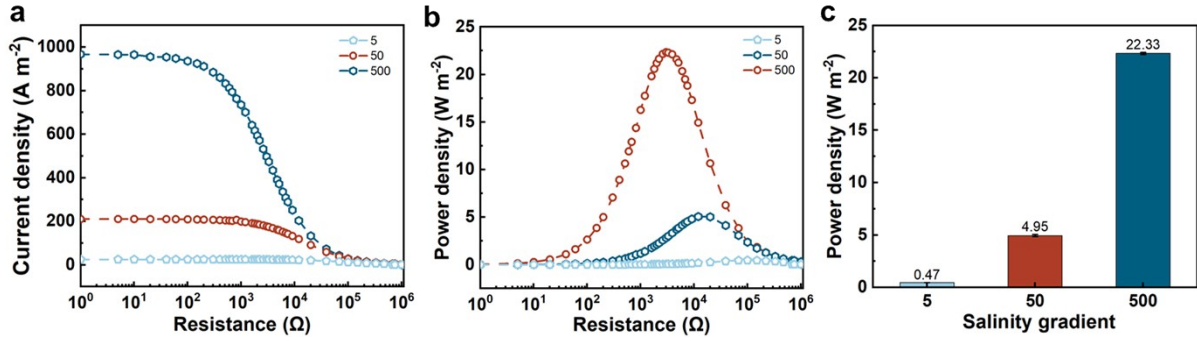
Fig. S16. (a) The current density decreases with increasing external resistance at 5-fold, 50-fold and 500-fold concentration gradients. (b) The output power density increases firstly and then decreases with increasing external resistance. (c) Maximum power density at three concentration gradients. The 500 nm microfluidic ANF film results a power density around 22.33 W m^{-2} maximum in a NaCl solution with a 500-fold salinity gradient.
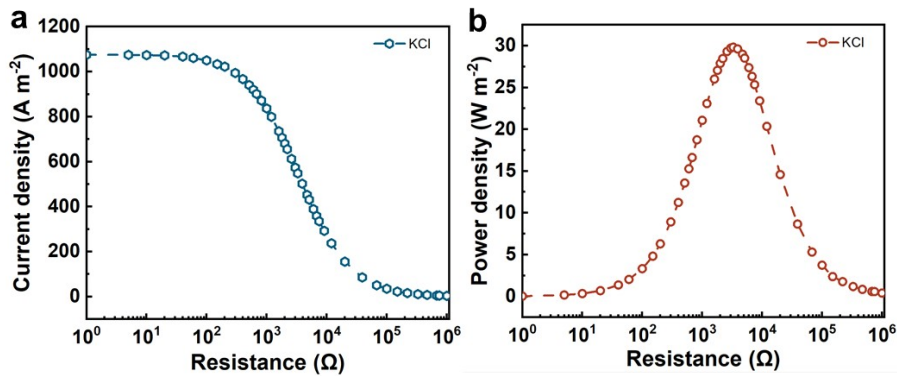

Fig. S17. (a) Current density and (b) power density in 500-fold concentration of KCl solution. The 500 nm microfluidic ANF film results a power density can reach 29.83 W m^{-2}.
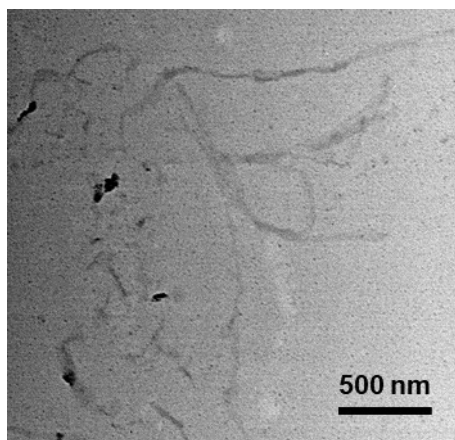

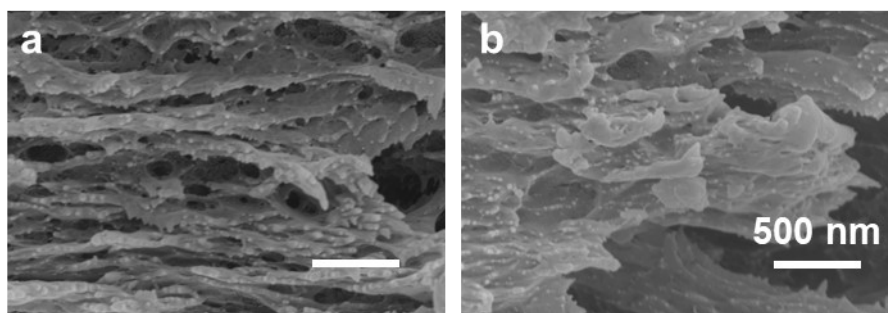**Fig. S18**. TEM image of the regenerated cellulose nanofibers.

Fig. S19. Zoomed SEM images of the fracture features for regenerated cellulose nanofiber films. (a) Microfluidic based fabricated film. (b) Casted film.
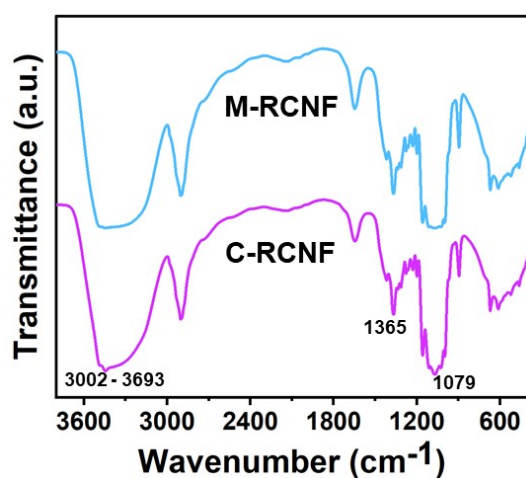

Fig. S20. FTIR spectra of the RCNF films from microfluidic and casting methods.

References

1. Y. Choi, G. Shin, J. G. Jeon, J. H. Kim, J. H. Lee, H. J. Kim, B. J. So, Y. Han and T. J. Kang, *Mater. Lett.*, 2024, **362**, 136185.

2. N. Yan, Z. Li, X. Chai and Z. Lu, *J. Ind. Eng. Chem.*, 2024, **134**, 425-431.

3. C. Torres, O. Valerio, R. T. Mendonça and M. Pereira, *Int. J. Biol. Macromol.*, 2024, **267**, 131587.